42nd AIAA Aerospace Sciences Conference and Exhibit
January 5-8, 2004, Reno, NV

AIAA-2004-0966

DESIGN OF A MICROGRAVITY SPRAY COOLING EXPERIMENT

Kerri M. Baysinger*, Kirk L. Yerkes†, and Travis E. Michalak‡
Air Force Research Laboratory, AFRL/PRPS,
Wright-Patterson Air Force Base, Ohio 45433
Richard J. Harris§
University of Dayton Research Institute,
300 College Park Avenue, Dayton, Ohio 45469
and
John McQuillen¶
NASA Glenn Research Center, Cleveland, Ohio 44135

ABSTRACT

An analytical and experimental study was conducted for the application of spray cooling in a microgravity and high-g environment. Experiments were carried out aboard the NASA KC-135 reduced gravity aircraft, which provided both the microgravity and high-g environments. In reduced gravity, surface tension flow was observed around the spray nozzle, due to unconstrained liquid in the test chamber and flow reversal at the heat source. A transient analytical model was developed to predict the temperature and the spray heat transfer coefficient within the heated region. Comparison of the experimental transient temperature variation with analytical results showed good agreement for low heat input values. The transient analysis also verified that thermal equilibrium within the heated region could be reached during the 20-25s reduced gravity portion of the flight profile.

NOMENCLATURE

b	= pedestal radius, 0.0085m
A	= cross sectional area of pedestal, m
c	= thickness (z direction) of region 3, 0.08m
F_1, F_2	= intermediate functions
H	= h / k
h	= heat transfer coefficient, W/m^2-K
J_o, J_1	= Bessel Functions
k	= thermal conductivity, W/m-K
l	= thickness (z direction) of region 2, 0.001m
g	= heat generation, Q/V_1, W/m^3
Q	= input heat, W
f	= fraction of Q lost to the support structure
Q_1	= f (Q/A), W/m^2
r	= radial distance, m
T	= temperature, K
T'	= transient temperature, region 2, K
t	= time, s
V_1	= heater volume, m^3
z	= vertical distance, m
α	= thermal diffusivity, m^2/s-K
$\beta,\gamma,\eta,\varphi$	= Eigenvalues
δ	= thickness (z direction) of region 1, 1.0e-6m
θ	= temperature transformation (T_3- T_∞), K
ϕ_1,ϕ_2	= intermediate functions

Subscripts

1	region 1 of model (heater film)
2	region 2 of model (fused silica substrate)
3	region 3 of model (polycarbonate pedestal)
∞	bulk fluid properties
i	initial properties
m,n,s,p	index integers
SS	steady state properties

INTRODUCTION

The dissipation of thermal energy from current and future electronics for proposed high power space based concepts has resulted in the development of thermal management approaches tailored for high heat flux acquisition and high thermal energy transport. To be effective, these proposed thermal management approaches must operate in extreme space environments. Several thermal management approaches have been or are being considered for space environments such as jet impingement[1], two phase flow and heat transfer[2], pool boiling[3,4,5], and spray cooling[6].

An analytical and experimental study performed by Labus[1] determined the free surface shape of a jet impinging on an unheated flat disk in microgravity, Fig.1. For flows in which the viscosity effects were negligible compared to the effects from surface tension and inertial forces, there were three flow regimes; surface tension flow, transitional flow, and inertial flow. These flow regimes were correlated to Weber number and the ratio of jet radius to disk radius.[1]

*Masters candidate, Wright State University, Department of Mechanical and Materials Engineering, Dayton OH.
† Research Engineer/Scientist.
‡Associate Mechanical Engineer.
§Research Engineer. Member AIAA.
¶Aerospace Engineer, Microgravity Fluid Physics Branch

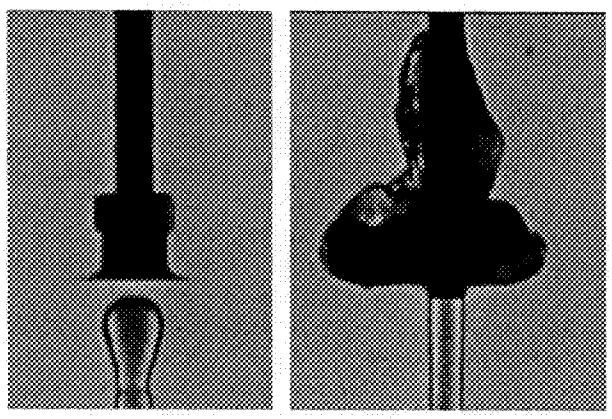

Fig. 1 Surface tension flow for jet impingement in microgravity[1].

There have been many microgravity studies focused on the physics involved in two-phase flow with heat transfer that have been performed in drop towers, reduced gravity aircraft flights, and in-orbit experiments. Two-phase, one-component flow with heat transfer in microgravity is seen in many thermal management systems such as heat pipes, loop heat pipes, and capillary pumped loops. Work has been done to try to use similarity considerations to scale terrestrial models to predict the behavior of, and to design, prototypes for microgravity.[2]

Microgravity research on pool boiling with and without subcooling has been performed by many researchers[3,4,5]. It has generally been found that microgravity conditions do not significantly change the heat transfer coefficient for nucleate boiling. However, the Critical Heat Flux (CHF) is generally reduced in microgravity. This reduction in the CHF is, in part, a result of the variation in bubble dynamics in microgravity due to the lack of buoyancy forces.[5] The observations by Kim et.al.[4] showed that small bubbles will coalesce into a large bubble on the surface of the heater in reduced gravity. During subcooled boiling, thermocapillary flows can develop around bubbles forcing the bubble to the heater surface while drawing warm liquid away from the heater and cool liquid to the heater.[5]

Many researchers have investigated the utility of two-phase sprays for the thermal management of devices generating high heat fluxes; however, there has been little research addressing the physics and ultimate performance of two-phase spray cooling in the microgravity environment. The development of concepts such as spray cooling in microgravity must be supported with a sound understanding of the micro- and macro-scale two-phase spray thermophysics.

Several microgravity spray cooling experiments were performed by Yoshida[6] and Kato[7]. The experiments looked at both transient and steady state spray cooling in microgravity during reduced gravity aircraft flights. A copper block heater was used for transient heat transfer experiments, and a clear thin film ITO heater on a clear base was used for steady state experiments with flow visualization. The volumetric spray fluxes used were between 0.000136 and 0.000370 m^3/m^2-s. These fluxes were low enough that a continuous film of coolant was not allowed to develop on the heater surface. The Weber numbers for their experiments ranged from 28 to 622, with all but two of the experimental cases having Weber numbers below 60.[6]

Fluid management issues that would be encountered for a continuous-flow, closed-loop microgravity spray cooling system were not addressed. No attempt was made during the experiments to retrieve and reuse the working fluid in a closed-loop system.

The objective of this paper is to present the design and preliminary testing of a microgravity spray cooling experiment. Tests were conducted aboard the NASA KC-135 reduced gravity aircraft, which provided both microgravity and high-g (approximately 1.8g) environments by following a parabolic flight trajectory. To build on the work of the previously mentioned researchers, the primary purpose of this study is to address heat transfer and fluid management for a continuous-flow, closed-loop microgravity spray cooling system. Emphasis is placed on developing a transient analytical model to predict temperatures and the spray heat transfer coefficient within the heated region of the experiment. Flow rate was sufficient to keep the heater surface completely immersed in the working fluid.

EXPERIMENTAL SETUP

The experiment consists of two primary components as shown in Fig. 2. The first component is a rotatable spray test chamber containing the spray nozzles, heaters, primary condenser surface, and two sump configurations to collect the liquid and condensate. The second component is the flow loop system that consists of two flow loops: 1) a FC-72 loop to manage the working fluid and 2) a water loop to cool the spray test chamber.

The experiment was operated by applying electrical power to the Indium Tin Oxide (ITO) heaters, to generate heat, and spray cooling the heaters. Data was acquired and the status of the experiment was monitored using thermocouples, pressure transducers, and flow meters placed throughout the experimental apparatus.

Design of the experimental system was accomplished using SolidWorks 3D modeling software. In addition, preliminary heat transfer analyses of the chamber, fluid loops, and sumps were performed

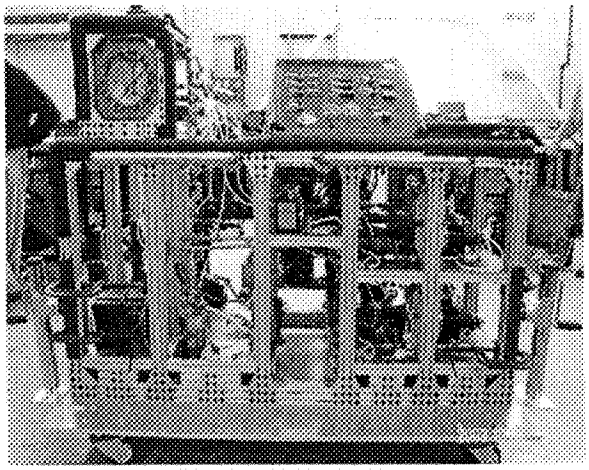

Fig. 2 Experimental apparatus.

using analytical and numerical methods. Results of these analyses were used to determine chamber size, locations of the greatest temperature gradients within the heater support structure for thermocouple placement, and to define the uncertainty in heat loss measurements through the heated region.

The experiment framework was constructed from "2020" and "1010" sizes of aluminum extrusions and hardware from 80/20, Inc. Shelves were constructed of ¼"-thick aluminum and installed for the purpose of mounting equipment. The entire frame rested on a ½"-thick aluminum plate, which served both as a mounting plate and a spill containment pan.

Detailed structural analysis and testing were conducted to satisfy NASA safety requirements. Structural integrity at various g-loads was evaluated for flight on the KC-135 aircraft. NASA guidelines required that all framework and equipment be able to withstand a 9-g load in the forward direction, 3-g in the aft, 6-g down, 2-g lateral, and 2-g up. In addition, a factor of safety of 2 was required, so all structural analysis and testing were performed at twice the given requirements. Much of the smaller equipment installed on the experiment was pull-tested using a load cell, however, larger items and the frame itself were analyzed using static equilibrium equations.

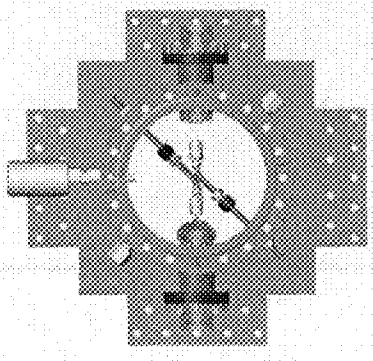

Fig. 3 Spray test chamber.

A. Spray Chamber

The spray test chamber, as shown in Fig. 3, consisted of two opposed spray nozzles, heaters, and sump systems. Various nozzles were evaluated using a two-axis Dantec Phase Doppler Anemometer to determine spray uniformity and droplet size distribution. Typical droplet velocity, volumetric flux, and droplet size distributions for the selected nozzles (FullJet 1) by Spraying Systems, are shown in Figs. 4-6.

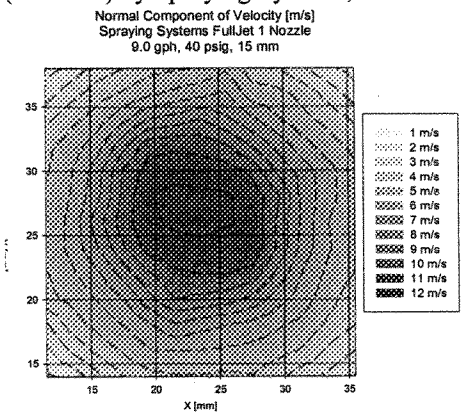

Fig. 4 Nozzle droplet velocity distribution.

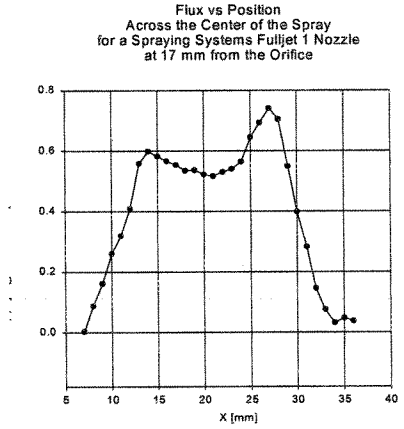

Fig. 5 Nozzle volumetric flux vs. position

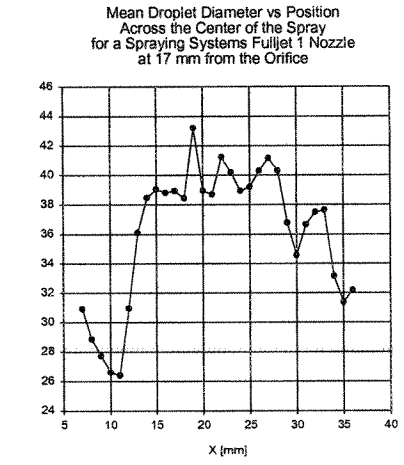

Fig. 6 Nozzle droplet diameter vs. position.

Transparent target ITO heaters were mounted on polycarbonate pedestals using Summers SK-9 optical cement and integrated into the sump, Fig. 7. The pedestals were cylindrical, with a radius of 8.5 mm. The nozzles and pedestals were positioned so as to minimize over-spray. The sumps served to remove excess fluid from the chamber and spray surface through an annulus between the heater pedestal and sump wall. Vapor generated at the heater surface was exhausted past the nozzle or entrained with the excess liquid through the sump annulus. The internal chamber wall was lined with two layers of stainless steel mesh (100 and 150 sizes). This provided a surface for condensation as well as a wick structure for condensate return to the sump.

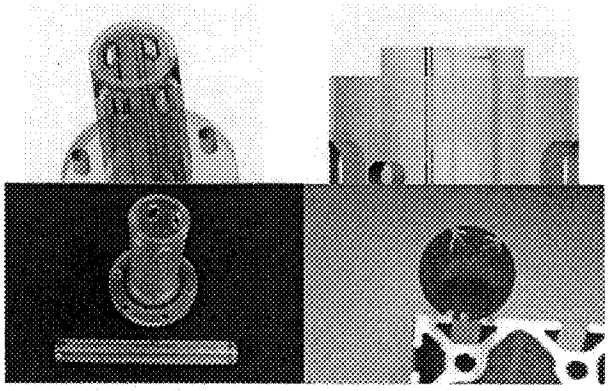

Fig. 7 Sump and pedestal.

The test chamber was affixed to a hinge line enabling it to be rotated so that the nozzles could be oriented in either a vertical or horizontal position. For these experiments, the chamber was positioned so that the nozzles remained in the vertical orientation. A pressure transducer was installed to measure the vapor pressure inside the chamber. The exterior surface of the chamber was cooled using a separate water cooling fluid loop. A tri-axis Columbia SA307HPTX accelerometer with an uncertainty of +/- 0.03g was mounted on the test chamber to record the transient variation in acceleration throughout the flight profile.

B. Fluid Loops

The two fluid loops are shown schematically in Fig. 8. The fluid loops served two primary purposes. The FC-72 loop recirculates the working fluid, and the water loop cools the exterior of the test chamber. The loops contain combinations of pumps, flow meters, pressure transducers, valves, pressure switches, reservoirs, and associated plumbing to monitor and direct fluid flow. Temperatures throughout the fluid loops were monitored using Type E, 0.0625" diameter, thermocouples.

i. FC-72 Loop

A positive displacement scavenging pump (Tuthill) was used to pump degassed FC-72 fluid from the sumps through a series of three air-liquid heat exchangers to a reservoir. The reservoir contained stainless steel wool to dampen fluid sloshing during the flight profile and serves as both a volume for the scavenging pump to dump excess working fluid and a pickup reservoir for the nozzle pumps. Following the reservoir, the fluid branched off into two identical flow paths, one for each

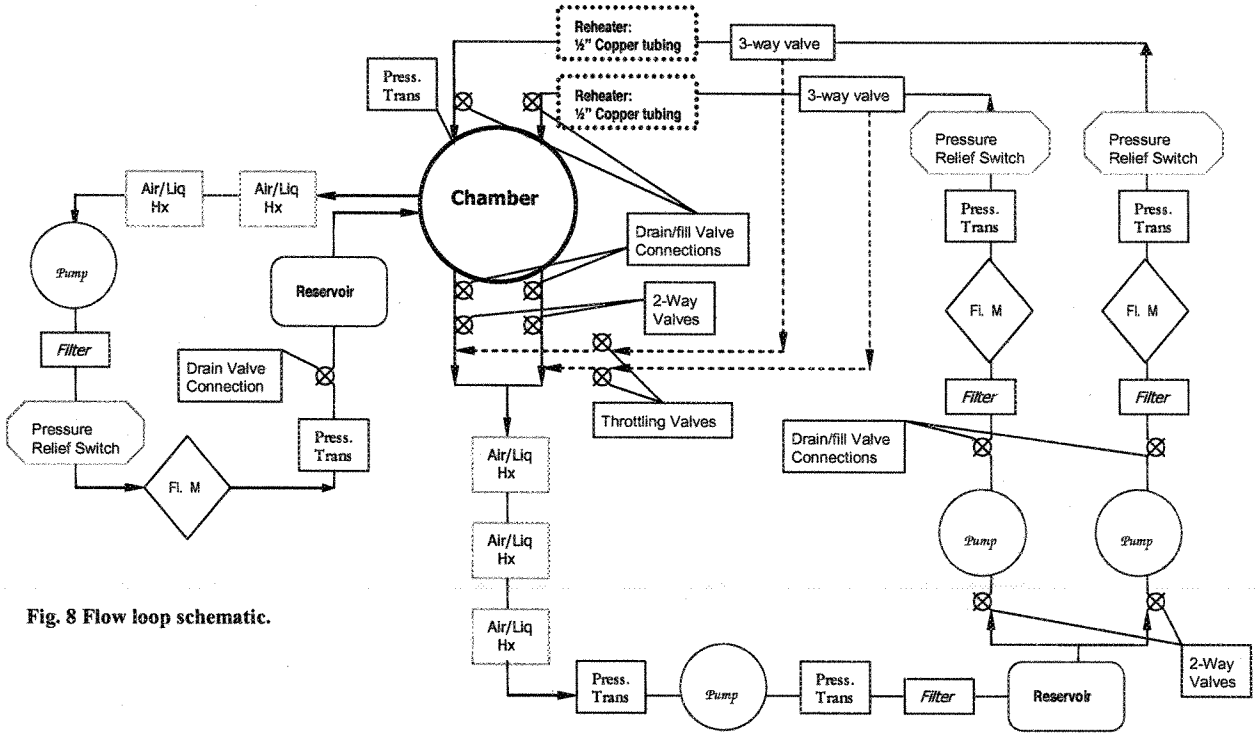

Fig. 8 Flow loop schematic.

nozzle. Each branch consisted of a positive displacement pump (Tuthill) followed by a 15-micron filter (Swagelock), flow meter (Omega), pressure transducer (Omega), and pressure switch (United Electric). Electrically-actuated ball valves (Hoke) were placed at the entrance and exit of each branch, to permit isolation of the test chamber. In addition, a length of copper tubing was placed in each branch to allow for future installation of a reheater that would maintain the spray at saturated conditions.

ii. Water Loop

The water loop is a single-phase loop that maintains the temperature of the exterior wall of the test chamber. This flow loop also incorporated two air-liquid heat exchangers, pump, filter, flow meter, reservoir, and pressure transducer. The reservoir also contained stainless steel wool to dampen fluid sloshing.

mounted to the top of the experimental package, coupled to an HP 34970A data acquisition/switch unit.

Temperature measurements were obtained throughout the chamber, heater pedestal, and within the sump annulus using sheathed thermocouples. Type E, 0.063"diameter (time constant <4.0s), thermocouples were placed in the chamber to measure chamber wall and vapor temperatures and Type E, 0.010"diameter (time constant < 0.5s), were mounted within the heater support structure. For additional stability and accuracy in temperature measurement, the thermocouples within the chamber and heater support structure were referenced to a Hart 9101 zero point reference junction with a stability of 0.005^{0}C.

Thermocouples within the heater support structure were used to determine the heat loss from the ITO heaters. Fig. 10 shows thermocouple locations within the heated pedestal. It must be noted that the temperatures at the heater surface and heater/fused silica interface were not measured and can only be

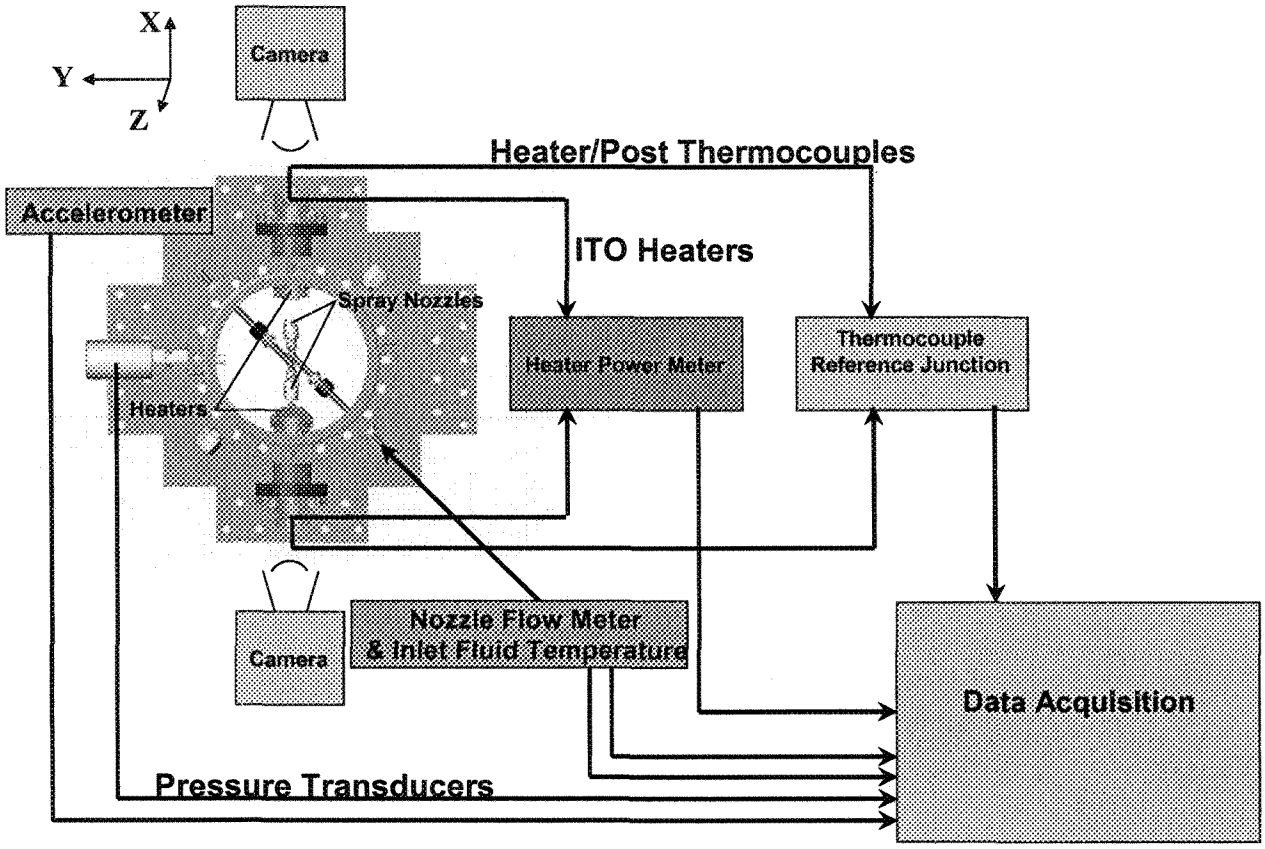

Fig. 9 Instrumentation schematic.

C. Instrumentation and Documentation

The experiment was operated and monitored via a control panel and data acquisition system. A diagram of the instrumentation system is shown in Fig. 9. The data acquisition system consists of a Dell laptop computer

inferred through analytical means. In addition, the ambient temperature was monitored using a Type E thermocouple and a YSI 44006 thermistor mounted on the experiment framework.

Thermocouples mounted within the chamber and support structure were calibrated using a Hart Scientific

model 5628 RTD temperature probe and Hart Scientific model 7320 temperature bath in the temperature range from 35° to 120°C. Resulting thermocouple calibrations yielded an uncertainty of +/- 0.02°C. A typical thermocouple calibration curve is shown in Fig. 11.

Heater power was monitored using power meters (Flex-Core) with an uncertainty of 2.5W. Visual documentation was acquired through the use of two Sony DCR-TRV33 video cameras mounted to the experimental frame. One camera recorded a full view of the test chamber, observing the behavior of the fluid therein. The second camera was positioned to record a field of view only of the nozzle being tested. When testing switched from one nozzle to the other, the camera position was adjusted to record the appropriate nozzle.

Top Pedestal Thermocouple Locations		
Thermocouple Number	Radial Location	z-location
	(m)	(m)
C8	0.004971	0.08
C10	0.004971	0.078755
C11	0.007518	0.078755
C12	Broken	
C13	Broken	
C14	0.007518	0.079746

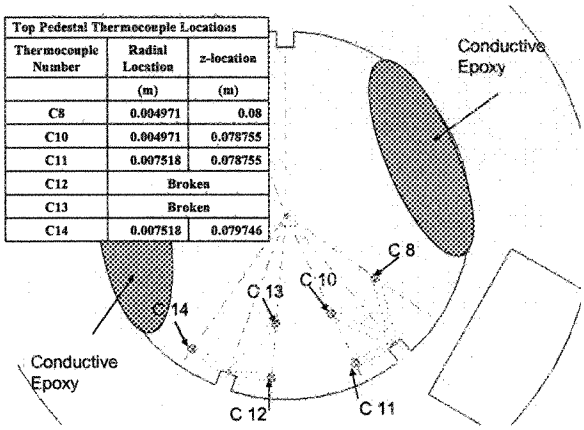

(a)

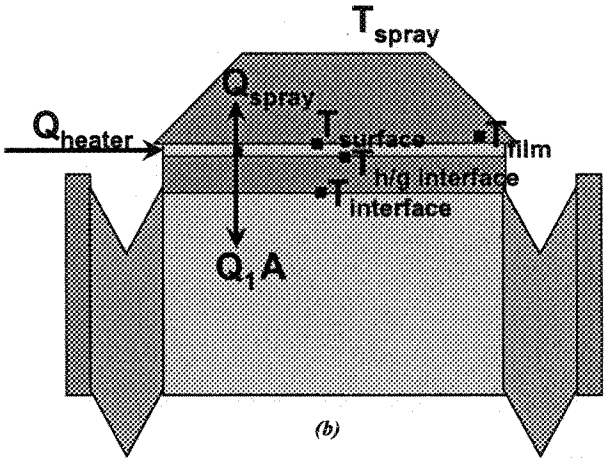

(b)

Fig. 10 Heater and heater support structure region a) radial and axial thermocouple locations b) schematic of heat and fluid flow paths with critical temperature locations.

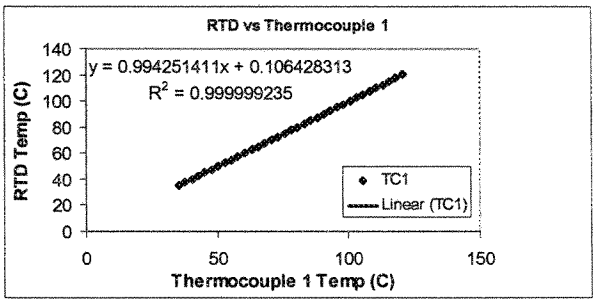

Fig. 11 Typical thermocouple calibration curve.

UNCERTAINTY ANALYSIS

An uncertainty analysis was conducted to determine the approximate magnitude of experimental error in determining the spray convective heat transfer coefficient at the surface of the ITO heater. Assuming one dimensional heat transfer for region 2, thin fused silica substrate,

$$Q_{heater} = Q_1 A + Q_{spray} = \frac{k_2 A}{l}(T_{h/g\,interface} - T_{interface}) + h_1 A(T_{surface} - T_{film}).$$

Furthermore, assuming steady state conditions where h_1 has no dependence on acceleration, experimental uncertainty can be approximated where

$$h_1 = \frac{Q_{heater} - \frac{k_2 A}{l}\left(T_{h/g\,interface} - T_{interface}\right)}{A\left(T_{surface} - T_{film}\right)} = \frac{Q_{heater} - Q_1 A}{A\left(T_{surface} - T_{film}\right)}$$

or

$$(h_1 A) = \frac{Q_{heater} - Q_1 A}{\Delta T}.$$

The relationship for rms error can be approximated using

$$E(h_1 A) = \left\{\left(\frac{\partial(h_1 A)}{\partial Q_{heater}}\Delta Q_{heater}\right)^2 + \left(\frac{\partial(h_1 A)}{\partial Q_1}\Delta Q_1 A\right)^2 + \left(\frac{\partial(h_1 A)}{\partial \Delta T}\Delta(\Delta T)\right)^2\right\}^{1/2}$$

with

$$\Delta T = 1K$$
$$\Delta(\Delta T) = 1K$$
$$\Delta Q_{heater} = 3W$$
$$\Delta Q_1 A = 0.03W.$$

The approximate rms error becomes

$$E(h_1 A) \approx 20\%.$$

ANALYSIS

The analysis of heat transfer to the spray and through the heater mounting structure was accomplished by accounting for three geometric regions in the heat transfer process. These regions are shown in Fig. 12 and consisted of the heater, fused silica mounting substrate to which the heater is attached, and the polycarbonate pedestal.

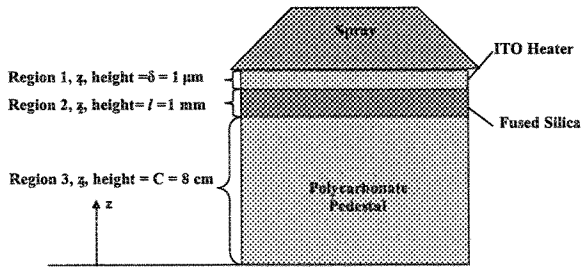

Fig. 12 Analytical domain for heater and heater support structure.

A. Region 1 The heater was treated as a thin, steady-state, one-dimensional conduction problem with internal heat generation. The top surface of the heater was treated as a convective boundary with the heat transfer coefficient resulting from the spray. The lower surface was treated as a flux boundary which is defined as the fraction of the heat generated that is not dissipated off of the top surface due to the spray cooling. The governing equation becomes

$$\frac{d^2T_1}{dz_1^2}+\frac{g}{k_1}=0, \quad 0\le z_1\le \delta, \tag{1}$$

with boundary conditions

$$\frac{dT_1}{dz_1}+H_1T_1=H_1T_\infty, \quad z_1=\delta \tag{1a}$$

$$\frac{dT_1}{dz_1}=\frac{Q_1}{k_1}, \quad z_1=0. \tag{1b}$$

The solution for the temperature distribution within the heater becomes

$$T_1(z_1)=-\frac{g}{2k_1}z_1^2+\frac{Q_1}{k_1}z_1+T_\infty + \frac{1}{h_1}\left[\frac{h_1 g}{2k_1}\delta^2+\left(g-\frac{h_1Q_1}{k_1}\right)\delta-Q_1\right], \quad 0\le z_1\le\delta. \tag{2}$$

B. Region 2 The fused silica substrate, to which the heater is attached, was treated as a transient, one-dimensional conduction problem

$$\frac{\partial^2T_2}{\partial z_2^2}=\frac{1}{\alpha_2}\frac{\partial T_2}{\partial t}, \quad 0\le z_2\le l \tag{3}$$

with boundary and initial conditions

$$\frac{dT_2}{dz_2}=\frac{Q_1}{k_2}, \quad z_2=0 \tag{3a}$$

$$T_2=T_1(z_1=0)= T_\infty+\frac{1}{h_1}\left[\frac{h_1}{2k_1}\delta^2+(g-\frac{h_1}{k_1}Q_1)\delta-Q_1\right], \quad z_1=l \tag{3b}$$

$$T_2(z_2,0)=T_i. \tag{3c}$$

The solution takes the form of a steady-state term and a transient term as defined by

$$T_2=T_{ss}+T'. \tag{4}$$

Each of these terms can be solved with governing equations and boundary conditions

$$\frac{d^2T_{ss}}{dz_2^2}=0, \quad 0\le z_2\le l \tag{5}$$

$$\frac{dT_{ss}}{dz_2}=\frac{Q_1}{k_2}, \quad z_2=0 \tag{5a}$$

$$T_{ss}=T_1(z_1=0), \quad z_2=l \tag{5b}$$

and

$$\frac{\partial^2T'}{\partial z_2^2}=\frac{1}{\alpha_2}\frac{\partial T'}{\partial t}, \quad 0\le z_2\le l \tag{6}$$

$$\frac{dT'}{dz_2}=0, \quad z_2=0 \tag{6a}$$

$$T'=0, \quad z_2=l \tag{6b}$$

$$T'(z_2,0)=T_i-T_{ss}, \quad 0\le z_2\le l. \tag{6c}$$

The solutions become

$$T_{ss}=\frac{Q_1}{k_2}z_2+T_1(z_1=0)-\frac{Q_1 l}{k_2} \tag{7}$$

and

$$T'(z_2,t)=\frac{2}{l}\sum_{m=1}^{\infty}\cos(\beta_m z_2)e^{-\alpha_2\beta_m^2 t} \bullet \left\{\begin{array}{l}\left(T_i-T_1(z_1=0)+\dfrac{Q_1 l}{k_2}\right)\dfrac{\sin(\beta_m l)}{\beta_m} \\ -\dfrac{Q_1}{k_2}\left[\left(\dfrac{\cos(\beta_m l)}{\beta_m^2}+\dfrac{l\sin(\beta_m l)}{\beta_m}\right)-\dfrac{1}{\beta_m^2}\right]\end{array}\right\} \quad (8)$$

respectively.

Combining Eqns. 4, 7, & 8, the temporal temperature distribution for region 2 becomes

$$T_2(z_2,t)=\left(\frac{Q_1 z_2}{k_2}+T_1(z_1=0)-\frac{Q_1 l}{k_2}\right) +\frac{2}{l}\sum_{m=1}^{\infty}\cos(\beta_m z_2)e^{-\alpha_2\beta_m^2 t}\left\{\begin{array}{l}\left(T_i-T_1(z_1=0)+\dfrac{Q_1 l}{k_2}\right)\dfrac{\sin(\beta_m l)}{\beta_m} \\ -\dfrac{Q_1}{k_2}\left[\left(\dfrac{\cos(\beta_m l)}{\beta_m^2}+\dfrac{l\sin(\beta_m l)}{\beta_m}\right)-\dfrac{1}{\beta_m^2}\right]\end{array}\right\}, \quad (9)$$

where β_m's are positive roots to $\cos\beta_m l = 0$.

C. Region 3 The polycarbonate pedestal was treated as a transient, two-dimensional conduction problem

$$\frac{\partial^2 T_3}{\partial r^2}+\frac{1}{r}\frac{\partial T_3}{\partial r}+\frac{\partial^2 T_3}{\partial {z_3}^2}=\frac{1}{\alpha_3}\frac{\partial T_3}{\partial t}, \quad 0\le z_3\le c \quad (10)$$

with boundary and initial conditions

$$T_3(z_3=c)=T_2(z_2=0) \quad (10a)$$

$$\frac{\partial T_3}{\partial z_3}=0, \quad z_3=0 \quad (10b)$$

$$\frac{\partial T_3}{\partial r}+H_3 T_3=H_3 T_\infty, \quad r=b \quad (10c)$$

$$T_3(z_3,0)=T_i, \quad 0\le z_3\le c. \quad (10d)$$

Making the transformation

$$\theta=T_3-T_\infty, \quad (11)$$

Eqn. 10 becomes

$$\frac{\partial^2\theta}{\partial r^2}+\frac{1}{r}\frac{\partial\theta}{\partial r}+\frac{\partial^2\theta}{\partial {z_3}^2}=\frac{1}{\alpha_3}\frac{\partial\theta}{\partial t}, \quad 0\le z_3\le c, \quad (12)$$

with boundary and initial conditions

$$\theta(z_3=c)=T_2(z_2=0)-T_\infty \quad (12a)$$

$$\frac{\partial\theta}{\partial z_3}=0, \quad z_3=0 \quad (12b)$$

$$\frac{\partial\theta}{\partial r}+H_3\theta=0, \quad r=b \quad (12c)$$

$$\theta(z_3,0)=T_i-T_\infty, \quad 0\le z_3\le c. \quad (12d)$$

The solution for Eqn. 12 takes the form of

$$\theta(r,z_3,t)=\theta_{SS}(r,z_3)+\theta_1(r,z_3,t) \quad (13)$$

with governing equations and boundary conditions

$$\frac{\partial^2\theta_{SS}}{\partial r^2}+\frac{1}{r}\frac{\partial\theta_{SS}}{\partial r}+\frac{\partial^2\theta_{SS}}{\partial {z_3}^2}=0, \quad 0\le z_3\le c \quad (14)$$

$$\theta_{SS}=T_2(z_2=0)-T_\infty, \quad z_3=c \quad (14a)$$

$$\frac{\partial\theta_{SS}}{\partial z_3}=0, \quad z_3=0 \quad (14b)$$

$$\frac{\partial\theta_{SS}}{\partial r}+H_3\theta_{SS}=0, \quad r=b \quad (14c)$$

and

$$\frac{\partial^2\theta_1}{\partial r^2}+\frac{1}{r}\frac{\partial\theta_1}{\partial r}+\frac{\partial^2\theta_1}{\partial {z_3}^2}=\frac{1}{\alpha}\frac{\partial\theta_1}{\partial t}, \quad 0\le z_3\le c \quad (15)$$

$$\theta_1(z_3=c)=0 \quad (15a)$$

$$\frac{\partial\theta_1}{\partial z_3}=0, \quad z_3=0 \quad (15b)$$

$$\frac{\partial\theta_1}{\partial r}+H_3\theta_1=0, \quad r=b \quad (15c)$$

$$\theta_1(r,z_3,0)=(T_i-T_\infty)-\theta_{SS}=F_1(r)F_2(z_3), \quad 0\le z_3\le c. \quad (16)$$

The steady-state solution becomes

$$\theta_{SS}(r,z_3)=[T_2(z_2=0)-T_\infty]\frac{2H_3}{b} \bullet\sum_{n=1}^{\infty}\frac{J_o(\gamma_n r)\cosh(\gamma_n z_3)}{J_o(\gamma_n b)\left({H_3}^2+{\gamma_n}^2\right)\cosh(\gamma_n c)}. \quad (17)$$

The transient term takes the form

$$\theta_1(r,z_3,t)=\phi_1(r,t)\bullet\phi_2(z_3,t) \quad (18)$$

with the governing equations and boundary conditions

$$\frac{\partial^2\phi_1}{\partial r^2}+\frac{1}{r}\frac{\partial\phi_1}{\partial r}=\frac{1}{\alpha_3}\frac{\partial\phi_1}{\partial t},\quad 0\le r\le b \tag{19}$$

$$\frac{\partial\phi_1}{\partial r}+H_3\phi_1=0,\quad r=b \tag{19a}$$

$$\phi_1(r,0)=F_1(r)=1,\quad 0\le r\le b \tag{19b}$$

and

$$\frac{\partial^2\phi_2}{\partial z_3^{\,2}}=\frac{1}{\alpha_3}\frac{\partial\phi_2}{\partial t},\quad 0\le z_3\le c \tag{20}$$

$$\phi_2=0,\quad z_3=c \tag{20a}$$

$$\frac{\partial\phi_2}{\partial z_3}=0,\quad z_3=0 \tag{20b}$$

$$\phi_2(z_3,0)=F_2(z_3)=(T_i-T_\infty)-\theta_{SS},\quad 0\le z_3\le c. \tag{20c}$$

The solutions for Eqns. 19 and 20 become

$$\phi_1=\frac{2H_3}{b}\sum_{s=1}^{\infty}\frac{J_o(\eta_s r)e^{-\alpha_3\eta_s^2 t}}{J_o(\eta_s b)\left(H_3^{\,2}+\eta_s^{\,2}\right)} \tag{21}$$

and

$$\phi_2=\frac{2}{c}[(T_i-T_\infty)-\theta_{SS}]\sum_{p=1}^{\infty}\frac{1}{\varphi_p}e^{-\alpha_3\varphi_p^2 t}\cos(\varphi_p z_3)\sin(\varphi_p c) \tag{22}$$

respectively.

Combining Eqns. 11,13, and 18, final solution becomes

$$T_3(r,z_3,t)=\theta_{SS}(r,z_3)+\phi_1(r,t)\bullet\phi_2(z_3,t)+T_\infty. \tag{23}$$

Inserting solution from Eqns. 21 & 22 into 23,

$$T_3(r,z_3,t)=\theta_{SS}(r,z_3)+\left[\begin{array}{l}\dfrac{4H_3}{bc}[(T_i-T_\infty)-\theta_{SS}(r,z_3)]\\ \bullet\displaystyle\sum_{s=1}^{\infty}\sum_{p=1}^{\infty}\frac{J_o(\eta_s r)e^{-\alpha_3(\eta_s^2+\varphi_p^2)t}\cos(\varphi_p z_3)\sin(\varphi_p c)}{\varphi_p J_o(\eta_s b)\left(H_3^{\,2}+\eta_s^{\,2}\right)}\end{array}\right]+T_\infty, \tag{24}$$

where θ_{ss} is given in Eqn. 17 and the eigenvalues are positive roots to

$$\gamma_n's\Rightarrow H_3J_o(\gamma_n b)=\gamma_n J_1(\gamma_n b) \tag{24a}$$

$$\eta_s's\Rightarrow H_3J_o(\eta_s b)=\eta_s J_1(\eta_s b) \tag{24b}$$

$$\varphi_p's\Rightarrow\cos(\varphi_p c)=0. \tag{24c}$$

Equation 24 can be solved by assuming h_1, h_3, and Q_1. It should be noted that the interface temperature boundary conditions in regions 2 (Eqn, 3a) and 3 (Eqn. 10a) are evaluated using Eqns. 2 and 9.

RESULTS AND DISCUSSION

At the beginning of each test the data acquisition program was initiated via laptop, and all cameras, timers, etc., were synchronized and started. The data acquisition system monitored and recorded flow rate, acceleration, input heat, and temperatures for the duration of the flight. Temperatures were measured at the interface of the fused silica and polycarbonate pedestal (C8), within the polycarbonate pedestal (C10, C11, C14), at the inlet of the nozzle, and in the liquid film exiting the heater surface. Application of heater power was limited to less than 20W to evaluate the ability to maintain constant and control of the flow rate throughout the flight profile.

Figure 13 shows a typical flight profile with turns before and after a series of parabolas. This figure also shows the variation in ambient cabin temperature which is consistent with variation in aircraft altitude during maneuvering.

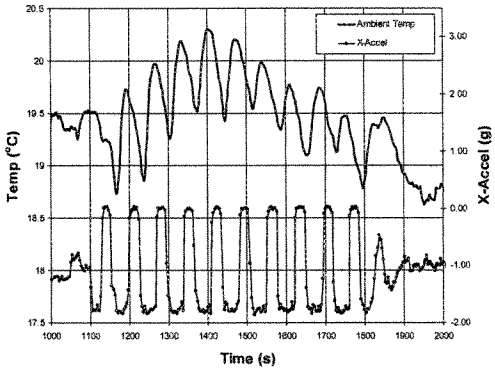

Fig. 13 Typical flight profile with ambient temperature and acceleration vs. time

During the reduced gravity portion of the flight, significant surface tension flow was observed around the nozzle and the sump inlet. It appeared that this flow was due to both the unconstrained liquid feeding up the exterior of the sump wall and a portion of the nozzle flow reversing direction and exiting out of the sump

inlet. This flow reversal appeared to be dependent on nozzle flow rate and occurred after impacting the heater surface and interior wall of the sump. Figure 14 shows typical surface tension flow around a nozzle and sump during the reduced gravity portion of the flight.

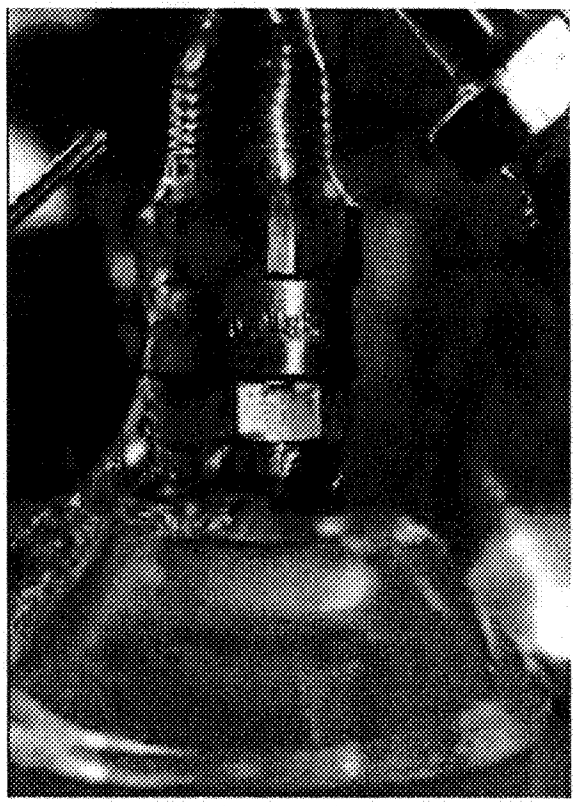

Fig. 14 Surface tension flow around the spray nozzle.

Figure 15 shows a typical transient variation in temperature to a linearly ramped increase in input heater power to 10.6W and an initial flow rate of 5gph. Also shown in Fig. 15 is the nozzle flow rate and vertical acceleration. For this case, the temperature within the heater support structure increased with an increase in heat and remained relatively constant until the flow rate decreased midway through the reduced gravity portion of the trajectory. With the decrease in flow, the heater support structure increased in temperature. With the exception of diminished flow rate there was no noticeable effect of the reduced gravity for this low heat input case. It should be noted that variations in flow rate were not limited to the reduced gravity portion but were also observed during the 1.8-g portion of the flight.

Equation 24 was solved analytically while varying the spray heat transfer coefficient, h_1, the pedestal wall heat transfer coefficient, h_3, and the fraction of heat loss, f, to the heater support structure. The initial temperature and film temperature were set to T_i = 22.5^{0}C and T_{film}= T_∞= 23.8^{0}C respectively. Figures 16-19 compare results of these analytical calculations to the experimental results for various temperatures located within the pedestal. This demonstrates that these analytical calculations can be used to evaluate and infer the correct magnitude of heat transfer coefficients assuming a fraction of heat is lost to the heater support structure.

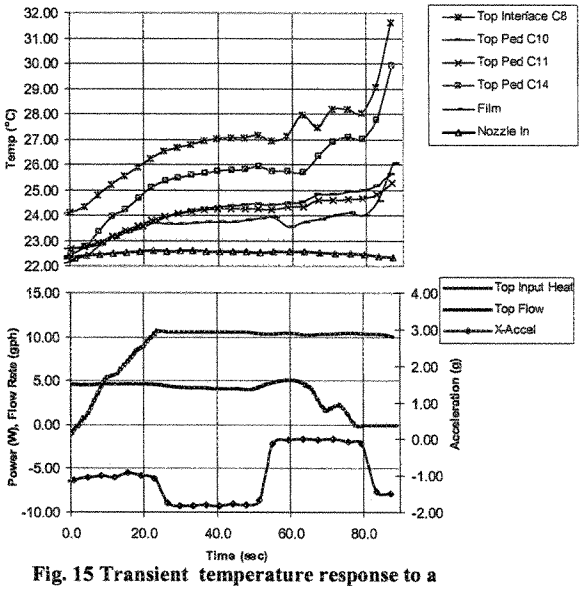

Fig. 15 Transient temperature response to a ramped heat input to 10.6W.

The analytical solutions shown in Figures 16-18 were calculated using a 10.6W step change in the heat input, while the experimental heat input actually varied as a ramp function up to 10.6W. As a result of this variation of heat input with time, only the steady-state solutions can be compared. Figure 16 shows the effect of varying the spray heat transfer coefficient, h_1=18,000, 22,000 W/m^2-K, while fixing the pedestal wall heat transfer coefficient, h_3=250 W/m^2-K, and fraction of heat lost, f=0.01, to the heater support structure. The discrepancy between analytical steady state solution and experimental results is consistent with variation in the spray heat transfer coefficient and the ability to reject sufficient heat from the heater surface to maintain the desired temperature distribution in the heater and heater support structure. Figure 17 shows the effect of varying the pedestal wall heat transfer coefficient, h_3=200,300 W/m^2-K, while fixing the spray heat transfer coefficient, h_1=20,000 W/m^2-K, and fraction of heat lost, f=0.01, to the heater support structure. For the case h_3=300 W/m^2-K, heat transfer increased resulting in the reduction in the pedestal temperature. Figure 18 shows the effect of varying the amount of heat lost, f=0.005, 0.05, to the heater support structure. The pedestal wall heat transfer coefficient and spray heat transfer coefficients were fixed to h_3=250 W/m^2-K and h_1=20,000 W/m^2-K respectively.

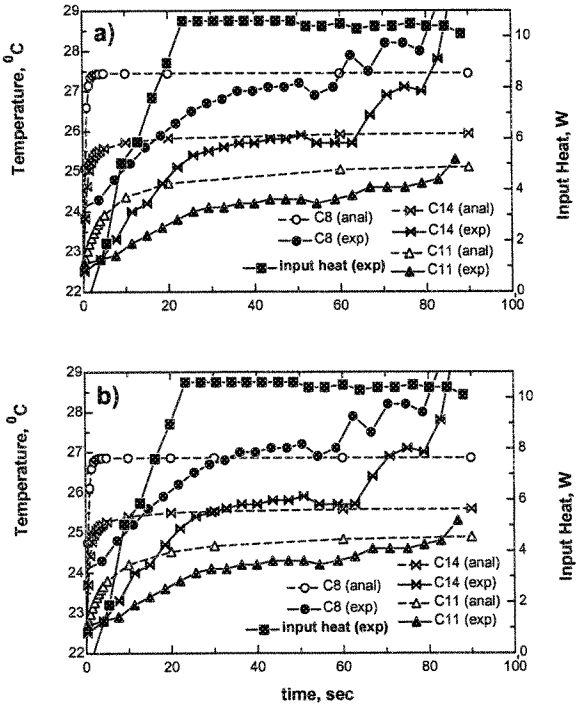

Fig. 16 Comparison of analytical calculation results to experimental results a) h_1=18,000, h_3=250, f=0.01 b) h_1=22,000, h_3=250, f=0.01.

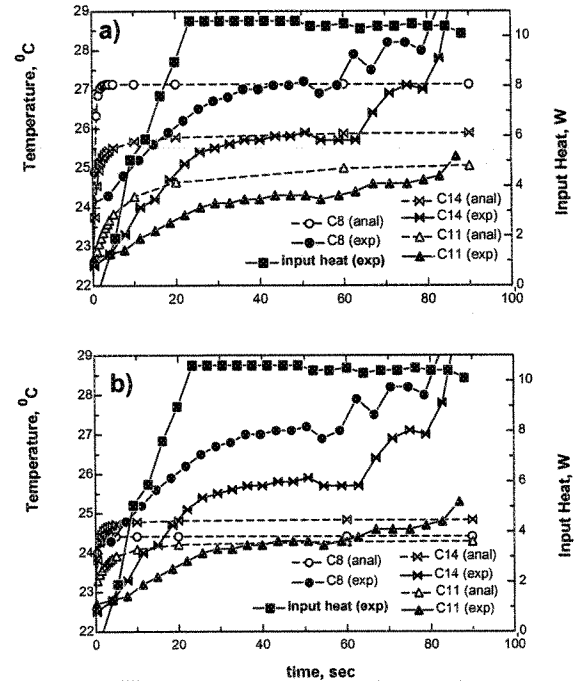

Fig. 17 Comparison of analytical calculation results to experimental results a) h_1=20,000, h_3=200, f=0.01 b) h_1=20,000, h_3=300, f=0.01.

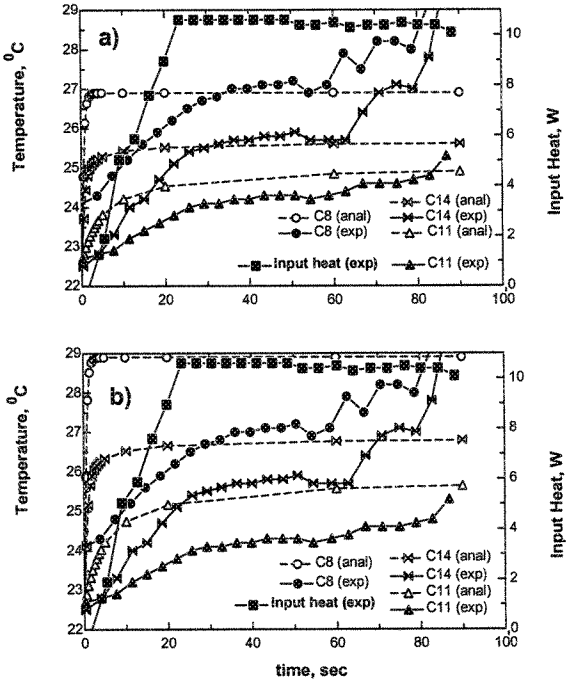

Fig. 18 Comparison of analytical calculation results to experimental results a) h_1=20,000, h_3=250, f=0.005 b) h_1=20,000, h_3=250, f=0.05.

As expected, the greater the fraction of heat loss to the heater support structure the greater the temperature within the pedestal.

Finally, Fig. 19 addresses the transient response in temperature when the heat input is treated either as a step input to 10.6 W or a ramped input following the function $Q = 0.488(t - t_1)$. Time t_1 is a time delay of 1.68s prior to the initiation of the input heat. This time delay matches the time delay observed with the experiment. For this case, the spray heat transfer coefficient, pedestal wall heat transfer coefficient, and fraction of heat lost to the heater support structure were fixed to h_1=20,000 W/m^2-K, h_3=250 W/m^2-K, and f=0.01 respectively.

Modeling the heat input as a ramped function showed good agreement with the transient portion of the experiment. There was a slight shift between the analytical calculations and experimental results possibly due to the added thermal mass of the conductive epoxy at the heater surface. Additional error in the thermocouple locations as well as the fact that the heater will not generate a uniform heat flux, due to the circular geometry, may also contribute to the discrepancy. In addition, this transient analysis enables the transient response of the experiment to be evaluated in comparison to the typical time scale encountered during the flight tests. The thermal time constant of the heater and heater support structure was found to be on

the order of 5-10s, for a step heat input. This ensures that the thermal response time of the heater and heater support structure was sufficiently fast to keep up with the transient nature of the flight profile.

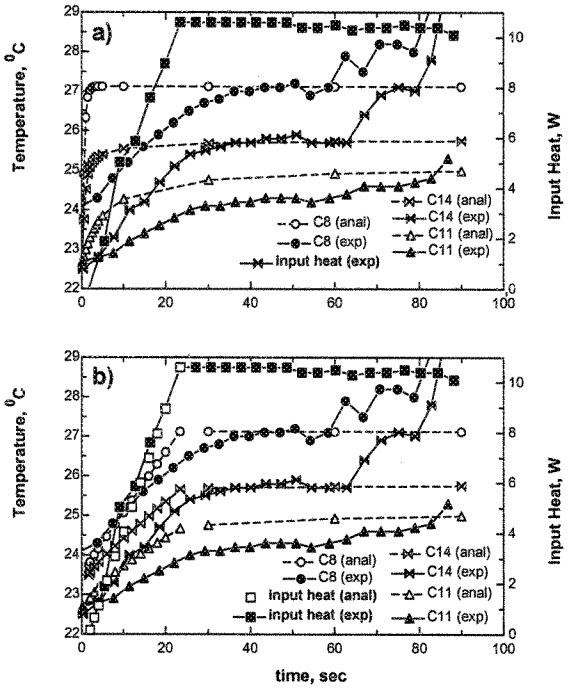

Fig. 19 Comparison of analytical calculation results to experimental results, h_1=20,000, h_3=250, f=0.01 a) step heat input to 10.6W b) ramped heat input, Q=0.488(t-t_1).

CONCLUSION

The initial design and operation of a spray cooling experiment in a microgravity environment has been completed. Without heating or with low input heat, surface tension flow dominated the fluid physics around the nozzle outlet and sump inlet. This surface tension flow may be reduced by redesigning the chamber wall to help further contain liquid within the test chamber. At the low heat loads tested, there were no observable effects due to either the reduced gravity or the 1.8-g portion of the flight profile. However, the flow rate fluctuations during each trajectory affected the cooling of the ITO heater. In order to maintain temperature control of the heat source, proper fluid management will be a critical challenge in both the reduced gravity and 1.8-g portions of the flight. Comparison of the transient temperature variation from the analytical formulation with experimental results showed good agreement for input heat loads less than 20W. The best agreement between transient analytical calculations and experimental results used a ramped heat input to simulate the experimental transient heat input. This resulted in 1%, f=0.01, of the heat input lost to the heater support structure with a spray heat transfer coefficient and pedestal wall heat transfer coefficient of h_1=20,000 W/m^{2}K and h_3=200-250 W/m^{2}k, respectively. Finally, the thermal time constant of the heater and heater support structure was found to be on the order of 5-10s, for a step heat input, which is less than the 20-25s period of reduced gravity per trajectory.

ACKNOWLEDGEMENTS

This research was conducted as part of the in-house program at the Air Force Research Laboratory, Propulsion Directorate, Power Division, Energy Storage and Thermal Sciences Branch, AFRL/PRPS, Wright Patterson Air Force Base, Ohio. The authors wish to thank 2nd Lt. Ryan C. Claycamp (USAF) for his contributions throughout the experimental process. The authors also wish to thank John E. Tennant (UES, Inc.) for his support in machining and assembling portions of the experimental apparatus.

REFERENCES

[1]Labus, T. L., "Liquid Jet Impingement Normal to a Disk in Zero Gravity," *NASA Technical Paper 1017*, 1977.

[2]Delil, A. A. M., "Microgravity two-phase flow and heat transfer," In: *Physics of Fluids in Microgravity* (Ed. Monti, R.), pp.263-292, Taylor & Francis, London, 2001.

[3]Kim, J. "Review of Reduced Gravity Boiling Heat Transfer: US Research," *J. Jpn. Soc. Microgravity Appl.*, Vol. 20, No. 4, pp 264-271, 2003.

[4]Kim, J., Benton, J.F., and Wisniewski, D., "Pool boiling heat transfer on small heaters: effect of gravity and subcooling," *International Journal of Heat and Mass Transfer* 45, pp 3919-3932, 2002.

[5]Straub, J. "Pool boiling and bubble dynamics in microgravity," In: *Physics of Fluids in Microgravity* (Ed. Monti, R.), pp.322-370, Taylor & Francis, London, 2001.

[6]Yoshida, K., Abe, Y., Oka, T., Mori, Y. H., Nagashima, A., "Spray Cooling Under Reduced Gravity Condition," *Journal of Heat Transfer*, Vol.123, pp.309-318, 2001.

[7]Kato, M., Abe, Y., Mori, Y. H., Nagashima, A., "Spray Cooling Characteristics Under Reduced Gravity," *Journal of Thermophysics*, Vol. 9., No. 2, Technical Notes, pp. 378-381, 1994.